

Human-Robot Navigation using Event-based Cameras and Reinforcement Learning

Ignacio Bugueno-Cordova^{1,3} Javier Ruiz-del-Solar^{1,2} Rodrigo Verschae³

¹Department of Electrical Engineering, Universidad de Chile

²Advanced Mining Technology Center (AMTC), Universidad de Chile

³Institute of Engineering Sciences, Universidad de O'Higgins

ignacio.bugueno@{ing.uchile.cl, uoh.cl} jruizd@ing.uchile.cl rodrigo@verschae.org

Abstract

This work introduces a robot navigation controller that combines event cameras and other sensors with reinforcement learning to enable real-time human-centered navigation and obstacle avoidance. Unlike conventional image-based controllers, which operate at fixed rates and suffer from motion blur and latency, this approach leverages the asynchronous nature of event cameras to process visual information over flexible time intervals, enabling adaptive inference and control. The framework integrates event-based perception, additional range sensing, and policy optimization via Deep Deterministic Policy Gradient, with an initial imitation learning phase to improve sample efficiency. Promising results are achieved in simulated environments, demonstrating robust navigation, pedestrian following, and obstacle avoidance. A demo video is available at the [project website](#).

1. Introduction

Reinforcement Learning (RL) addresses several applications from robotic manipulation to planning [8, 11, 19]. A key aspect is how an agent learns from environmental interactions, integrating rewards to develop a policy that maximizes cumulative rewards over time.

This work introduces a novel controller for human-centered robot navigation that integrates event-based vision and RL. In contrast to frame-based cameras, event cameras offer microsecond-level resolution, high dynamic range, and minimal motion blur [6], making them suitable for robot navigation and human tracking. The proposed framework combines data from event cameras, depth, and LIDAR sensors. It employs a two-stage learning process: an initial imitation learning (IL) phase generates a suboptimal policy, followed by refinement using Deep Deterministic Policy Gradients (DDPG). Pedestrian detection is performed using a YOLOv5s model trained on the PEDRo dataset with SAE

representations and a 10 ms event accumulation window.

The main contributions of this work are: i) the first integration of event-based vision with reinforcement learning for human-robot navigation; ii) a hybrid IL+RL training pipeline that reduces the learning time of the RL agent in a simulated environment; iii) a quantitative comparison of PD, IL, and RL controllers for person-following and obstacle avoidance.

The rest of this paper is organized as follows: Section 2 reviews related work; Section 3 introduces fundamental of event-based cameras and robot kinematics; Section 4 describes the proposed navigation framework; Section 5 presents the experimental results; and Section 6 concludes the paper and projects this work.

2. Related Work

2.1. Robot navigation using reinforcement learning

Recent advances in Deep Reinforcement Learning (DRL) have driven significant progress in Image-Based Visual Servo (IBVS) for robotics. In [18], the authors introduce a DRL-IBVS framework leveraging DDPGs to track dynamic objects in unmanned aerial vehicles. This method demonstrated effective object tracking validated in Gazebo simulations by directly mapping errors from the *bounding box* to linear velocity commands. In [1], the authors propose a collision-free IBVS approach with image plane trajectory planning to improve obstacle avoidance and maintain target visibility, focusing on the stability of system dynamics for mobile robots. Also, [12] addressed visibility constraints by introducing a DRL-based IBVS controller that adapts control gains, ensuring continuous visibility of a static object. Similarly, [17] developed a DDPG-based RL-IBVS controller for multirotor robots, showing the system's efficiency in object tracking tasks in simulated and real scenarios. Finally, [5] addressed parameter tuning within the visual servo of robots, proposing a DRL framework to optimize kinematic parameters dynamically in several tasks.

2.2. Reinforcement learning for robotics using event cameras

Event cameras have boosted deep learning applications in robotics by enabling fast response in complex environments. In [2], the authors focused on a precedent by integrating RL with event cameras for the first time in car-like robots, creating image-like features from event streams for tasks such as fast collision avoidance and obstacle tracking. On the other hand, [20] advanced the field in unmanned aerial vehicle (UAV) tracking by developing a deep reinforcement learning framework that maps event streams to drone control actions. Leveraging event cameras' high dynamic range and low latency, they achieved effective tracking in challenging conditions, including variable illumination, through domain randomization. Finally, [9] presented a detection and avoidance method for UAVs by directly processing individual events using a variational event-based autoencoder and a continuous-action RL controller. Their real-time obstacle avoidance system achieved higher success rates in navigation tasks than frame-based methods, highlighting the potential of event cameras in high-speed robotic applications.

3. Preliminaries

3.1. Event camera data

Event cameras respond asynchronously to brightness changes in the logarithmic intensity $L(\mathbf{u}_k, t_k) \doteq \log(I(\mathbf{u}_k, t_k))$ at pixel \mathbf{u}_k and time t_k . An event is triggered at $\mathbf{u}_k = (x_k, y_k)^T$ and t_k when brightness change surpasses a threshold $\pm C$, where $p_k \in \{-1, +1\}$ indicates polarity. Within a time window, the camera outputs an event sequence $\mathcal{E}(t_N) = \{(\mathbf{u}_k, t_k, p_k)\}_{k=1}^N$ with μs resolution [6].

3.2. Event data representation

Extracting useful information from event streams is imperative. Representations include: i) event frames (2D histograms), ii) temporal surfaces (2D pixel-wise timestamps), iii) voxel grids (3D spatio-temporal histograms), iv) reconstructed frames, among others [6]. One common method is the Surface of Active Events (SAE) [3, 14], dividing events by polarity. For each pixel (x, y) , the last event within a fixed interval Δt is scaled to $[0, 255]$, producing positive and negative channels:

$$\text{SAE}_{\text{neg/pos}}(x, y) = 255 \left(\frac{t_e - t_{\text{init}}}{\Delta t} \right). \quad (1)$$

Both channels combine to create a composite image $I_{\text{SAE}}(x, y)$, capturing recent activity.

3.3. Human-centered social robot

Bender [16] is a humanoid service robot from the University of Chile designed for human-robot interaction (HRI)

in domestic environments. The main idea behind Bender's design was to create an open and flexible research platform that offers human-like communication capabilities and empathy. Bender has an anthropomorphic upper body and a differential drive platform that provides mobility, as shown in Figure 1.

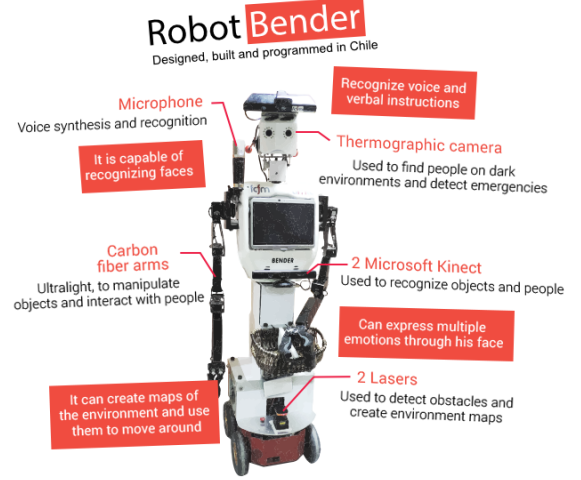


Figure 1. Bender: A General-Purpose Social Robot for Human-Robot Interaction [16].

Equipped with a Pioneer3AT [15], the robot platform allows a maximum linear acceleration of $2 [m/s^2]$ and angular acceleration of $5.24 [rad/s^2]$. For a $0.1[s]$ reaction time, velocity increments are limited at $0.2 [m/s]$ (linear) and $0.5 [rad/s]$ (angular) for navigation control design. Figure 2 provides a schematic of the robotic platform's kinematics.

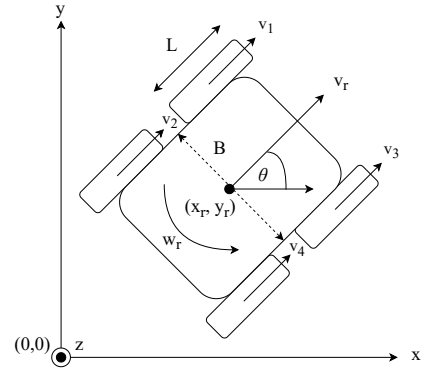


Figure 2. Kinematics of a four-wheel mobile robot.

In the illustration, (x_r, y_r) correspond to the coordinates of the midpoint between the driving wheels, θ is the orientation of the robot, $\{v_i\}_{i=1}^4$ and $\{\omega_i\}_{i=1}^4$ are the linear and angular speeds of the four wheels of the mobile robotic platform, B is the distance between the wheels, and L is the diameter of each wheel. It is assumed that the motion of the

robot is without slippage and also that $v_1 = v_2$, $v_3 = v_4$, $\omega_1 = \omega_2$, $\omega_3 = \omega_4$. Then, the kinematic model of the robot can be expressed as:

$$\begin{cases} \dot{x}_r = v_r \cos \theta, \\ \dot{y}_r = v_r \sin \theta, \\ \dot{\theta} = \omega_r, \end{cases} \quad (2)$$

where v_r is the linear velocity of the robot given by $v_r = \frac{L}{4}(\omega_1 + \omega_3)$, and ω_r is the angular velocity of the robot, expressed by $\omega_r = \frac{L}{2B}(\omega_3 - \omega_1)$. The state of the mobile robot is given by $q = [x_r, y_r, \theta]^T$, and the two control inputs are v_r and ω_r .

4. Proposed Framework

This section presents the proposed framework for human-robot navigation using event-based cameras and reinforcement learning. We introduce the pipeline of Figure 3, which includes: i) the sensors employed (event cameras, depth sensors, and obstacle detection), ii) a feature extraction module (in which an event-based pedestrian detector is employed), iii) the system state builder, iv) and the use of a model-free off-policy reinforcement learning algorithm (DDPG) for the adaptive calculation of the linear and angular velocities of the robotic platform.

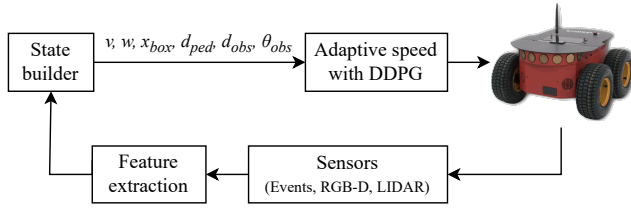


Figure 3. Human-robot navigation framework proposal.

4.1. Sensors on the mobile robotic platform

This work develops a controller for human-following in social robots, using a Pioneer 3-AT base equipped with a 2D Hokuyo LIDAR, DAVIS346 event camera, and RealSense camera mounted at 0.8 [m]. The vertically oriented cameras provide full-body pedestrian detection from 1 [m]. The controller prioritizes horizontal position (x_{bbbx}) from the DAVIS346 and distance (d_{ped}) from the RealSense, discarding vertical variability (y_{bbbx}) for stability. Depth tracking uses a homography to map event coordinates (x_{events}, y_{events}) from the DAVIS346 to the RealSense frame for pedestrian distance estimation:

$$\begin{bmatrix} x_{rgbd} \\ y_{rgbd} \end{bmatrix} = \text{tf}_{DAVIS \rightarrow RealSense} \begin{bmatrix} x_{events} \\ y_{events} \\ 1 \end{bmatrix}. \quad (3)$$

The LIDAR ensures obstacle avoidance within a 0.5-meter range. Figure 4 shows the sensor setup.

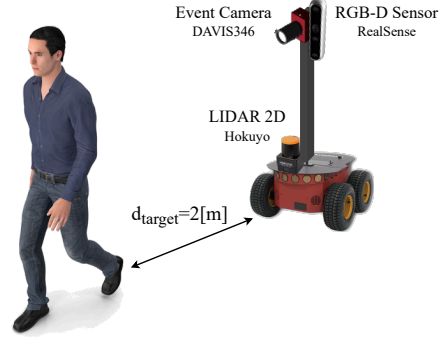


Figure 4. Sensor configuration on the Pioneer 3-AT platform. At the base: Hokuyo 2D (LIDAR). On top: A DAVIS346 (event camera) coupled with a Real Sense (RGB-D) sensor. The target distance between the mobile robotic platform and the pedestrian is 2[m].

4.2. Simulated scenario design

To exploit the high temporal resolution and non-motion blur of event cameras, a 21×12 [m²] scenario was designed, as shown in Figure 5. The map has wide corridors and obstacles, and the pedestrian moves at 0.7 [m/s]. The robot navigates a “figure-eight” trajectory, combining linear and angular movements over 100 seconds.

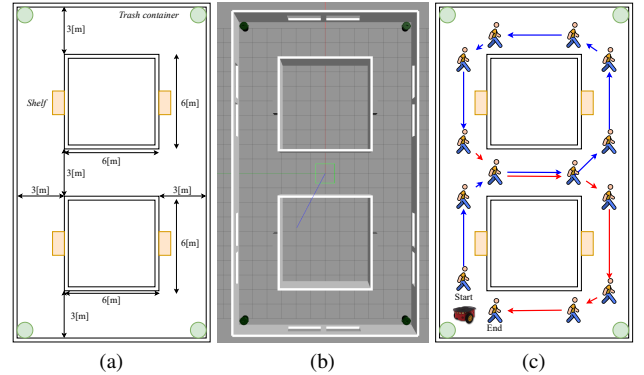


Figure 5. Simulated scenario design: (a) Scenario layout in Gazebo; (b) Scenario rendering; (c) Person's trajectory.

4.3. Using events for real-time navigation controllers

Event cameras operate asynchronously, eliminating the need for fixed-rate sampling and enabling continuous, low-latency sensing for navigation. This asynchronous nature allows data to be accumulated flexibly for perception, using either fixed-time windows, $\mathcal{E}_{\Delta t}(t) = \{e_k \mid t - \Delta t < t_k \leq t\}$, or fixed-event windows, $\mathcal{E}_N(t) = \{e_{k-N+1}, \dots, e_k\}$ as studied in [21]. These allow the system to adapt temporal resolution and data density according to the dynamics of the scene.

As a result, event data can be accessed and processed over arbitrary intervals, enabling the controller to “look back”

or “look ahead” in time. This supports adaptive inference: the controller can defer computation when activity is low, or update control actions more frequently during fast scene changes—improving responsiveness without increasing computational load.

4.4. Event-based pedestrian detection

To address the challenges of high-speed pedestrian detection (such as blur motion), this work proposes training YOLOv5s on the PEDRO database [4], a specialized event-based dataset designed for person detection in service robotics. The data was collected using a moving DAVIS346 event camera in a wide variety of scenarios and lighting conditions and is composed of: i) 119 recordings with an average duration of 18 seconds, ii) 43,259 bounding boxes manually annotated and iii) 27,000 samples.

Leveraging event cameras, which are significantly less prone to motion blur than conventional frame-based cameras [10], this work employs the SAE representation [3, 14] for enhanced detection accuracy, as shown in Figure 6.

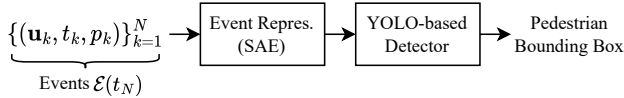


Figure 6. Event-based high-speed pedestrian detection pipeline.

YOLOv5s was selected due to its suitability for real-time applications, as the `small` variant is optimized for lightweight and fast inference on resource-constrained platforms. Although newer models like YOLOv9 or YOLOv11 may offer slightly better accuracy, state-of-the-art benchmarks [13] indicate that YOLOv5 achieves significantly faster inference times.

4.5. Imitation Learning of an PD-based navigation controller

We initially propose the design of a PD-based controller to calculate the Pioneer 3-AT’s velocities based on the bounding box position x_{bbox}, y_{bbox} of the person, with $x_{target} = 173, y_{target} = 140$. YOLO handles detection, RealSense provides distance to the pedestrian, and LIDAR ensures obstacle avoidance.

Now, the few successful expert trajectories generated by this controller are used to train an actor-network (MLP with six inputs and two hidden layers with 30 neurons) using Imitation Learning, with the state s comprising robot velocities, bounding box data, pedestrian distance, and the LIDAR sample. The 2D output adjusts linear and angular velocities, and training with Mean Squared Error (MSE) approximates expert actions, accelerating RL convergence in DDPG.

The selected objective function $\mathcal{L}(\theta)$ minimizes the difference between the predicted actions and the expert actions

Algorithm 1 Behavior Cloning

- 1: Obtain a dataset \mathcal{D} containing expert demonstrations
- 2: Initialize the policy π_θ with parameters θ
- 3: Select an ad-hoc objective function $\mathcal{L}(\theta)$
- 4: Optimize $\mathcal{L}(\theta)$ using the data contained in \mathcal{D}

in the dataset \mathcal{D} . It is defined as:

$$\mathcal{L}(\theta) = \frac{1}{N} \sum_{t=1}^N \|\pi_\theta(s_t) - a_t\|^2, \quad (4)$$

where N is the number of samples in a training batch, s_i represents the state, and a_i is the expert’s reference action for state s_i . The action predicted by the Actor-network for s_i , $\pi_\theta(s_i)$ corresponds to the action that the model attempts to approximate.

4.6. Reinforcement Learning for human-robot navigation

Reinforcement learning involves an agent learning to map situations to actions to maximize a reward, typically modeled as a Markov Decision Process (MDP). In this work:

1. The state $s_t = [v_r, w_r, x_{box}, d_{ped}, d_{obs}, \theta_{obs}]$ is a 6-dimensional vector that includes the robot’s linear and angular velocities, the center of the pedestrian’s bounding box, the distance to the person, and the distance d_{obs} and angle θ_{obs} to the closest obstacle detected by the LIDAR.
2. Actions $a_t = [\Delta v_r, \Delta w_r]$ are continuous increments for linear and angular velocities, applied every 0.1 seconds.
3. The reward function r_t encourages staying centered on the pedestrian and keeping a target distance of 2 [m]:

$$r_t = \begin{cases} 500, & \text{if } |e_x| < 1 \text{ pix and } |e_{d_{ped}}| < 0.1 \text{ m,} \\ -500, & \text{if } d_{obs} \leq d_{col,min}, \\ -500, & \text{if } d_{ped} > 3 \text{ m or } d_{ped} < 1 \text{ m,} \\ r_{t_{eq}} & \text{otherwise,} \end{cases} \quad (5)$$

where $r_{t_{eq}}$ penalizes deviations in centering and distance, defined as

$$r_{t_{eq}} = -k_{dist}|e_{d_{ped}}|^2 - \left(\frac{k_x}{1 + \alpha|e_{d_{ped}}|^2} \right) |e_x|^2, \quad (6)$$

with a factor α to adjust the influence of the centering error e_x when the distance error $e_{d_{ped}}$ is significant.

4.7. DDPG for Optimal Policy in RL

DDPG is a model-free, off-policy reinforcement learning algorithm designed for continuous action spaces well-suited for optimizing control policies like linear and angular velocities. In DDPG, actor-critic networks are used, where the actor-network $\mu(s|\theta^\mu)$ proposes actions, and the critic network $Q(s, a|\theta^Q)$ evaluates them. To stabilize training, each

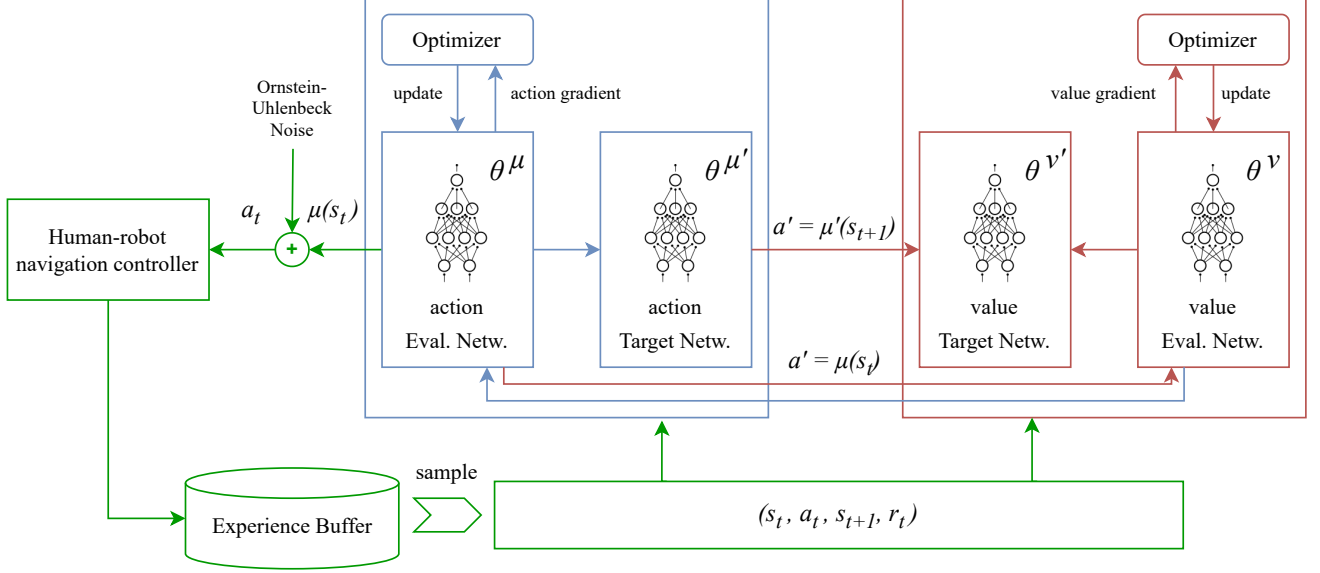


Figure 7. DDPG model-free algorithm applied to estimate velocity increments for robot navigation and human tracking. The state $s_t = [v_r, w_r, x_{\text{box}}, d_{\text{ped}}, d_{\text{obs}}, \theta_{\text{obs}}]$ includes the robot’s linear and angular velocities, the center of the pedestrian’s bounding box, the distance to the person, and the distance d_{obs} and angle θ_{obs} to the closest obstacle detected by the LIDAR. Based on [7].

network has a corresponding target network $\mu'(s|\theta^{\mu'})$ and $Q'(s, a|\theta^{Q'})$, updated incrementally to ensure slow changes that promote convergence:

$$\theta^{\mu'} \leftarrow \tau\theta^{\mu} + (1-\tau)\theta^{\mu'}, \quad \theta^{Q'} \leftarrow \tau\theta^{Q} + (1-\tau)\theta^{Q'}, \quad (7)$$

where τ is the update rate. The critic network is trained by minimizing the temporal difference loss:

$$L(\theta^Q) = \mathbb{E}_{\beta, p} \left[(Q(s_t, a_t|\theta^Q) - y_{i,t})^2 \right], \quad (8)$$

where the target value $y_{i,t}$ is calculated as:

$$y_{i,t} = r(s_t, a_t) + \gamma Q'(s_{t+1}, \mu'(s_{t+1}|\theta^{\mu'})|\theta^{Q'}). \quad (9)$$

Meanwhile, the actor network is updated by following the gradient:

$$\nabla_{\theta^{\mu}} J = \mathbb{E}_{s_t} [\nabla_a Q(s, a|\theta^Q) |_{a=\mu(s|\theta^{\mu})} \nabla_{\theta^{\mu}} \mu(s|\theta^{\mu})]. \quad (10)$$

The target networks are used to promote the convergence of the DDPG algorithm and serve as delayed copies of the original networks. The parameters of the target networks are updated as follows:

$$\theta^{\mu'} = \tau\theta^{\mu} + (1-\tau)\theta^{\mu'}, \quad \theta^{Q'} = \tau\theta^{Q} + (1-\tau)\theta^{Q'}, \quad (11)$$

where τ determines the update rate. A replay buffer is used to store and sample experience tuples (s_t, a_t, r_t, s_{t+1}) for uncorrelated training, enhancing learning stability. To encourage effective exploration in continuous spaces, Ornstein-Uhlenbeck noise is added to actions, providing temporally

correlated noise. The DDPG process is summarized in Figure 7 and Algorithm 2, illustrating its application to velocity control in human-robot navigation.

4.8. Training details

The simulated scenario uses Gazebo and ROS to conduct the training process. The models are implemented in Python, and the neural networks are built using the *PyTorch* framework. The episode will terminate and restart once these term states are found. In this work, the term states include the following:

1. The human reaches the final position.
2. Lose the feature in the camera’s field of view for more than 4 seconds.
3. The estimated distance between the camera and the person is greater than 3 [m] or less than 1 [m].
4. There is an obstacle at a distance of less than 0.5 [m].

Additionally, all DDPG neural networks have two hidden layers. The units for the first and second hidden layers are 30 and 30, respectively. The actor and target networks take the state as input and the 2-D action a_1, a_2 as output. The critical and target networks take the state-action pair 6-D (s, a) as input and the action value function 2-D $Q(s, a)$ as output. The activation functions used in the hidden layers of these neural networks are ReLU functions. In addition, modified tanh activation functions are added in the output layers of the actor and actor-target networks to ensure that their outputs are in the range $[-0.2, 0.2]$ for Δv_r and $[-0.5, 0.5]$ for Δw_r . The other parameters are reported in Table 1.

Algorithm 2 DDPG for human-robot navigation controller.

- 1: Initialize θ^μ with pre-trained weights from I.L.
 - 2: Initialize θ^Q randomly
 - 3: Initialize target networks by copying the original networks: $\theta^{\mu'} \leftarrow \theta^\mu, \theta^{Q'} \leftarrow \theta^Q$
 - 4: Initialize a noise generator Ω
 - 5: **for** episode = 1, ..., n **do**
 - 6: Randomly initialize the robot's position and observe the initial state s_1
 - 7: **for** $t = 1, \dots, n$ **do**
 - 8: Observe the state s_t of the environment
 - 9: Estimate the linear and angular velocity increments $\Delta v_r, \Delta w_r = \beta(s_t) = \mu(s_t|\theta^\mu) + \Omega_t$
 - 10: Compute the new linear and angular velocities
 - 11: Observe the reward r_t and the next state s_{t+1}
 - 12: Store the tuple (s_t, a_t, r_t, s_{t+1}) in the replay buffer M
 - 13: **if** s_{t+1} is a terminal state **then**
 - 14: **break**
 - 15: **end if**
 - 16: **if** M exceeds a threshold **then**
 - 17: Randomly sample N tuples (s_t, a_t, r_t, s_{t+1}) from buffer M to train the critic and actor networks according to Eq. 10
 - 18: Update the parameters of the target networks according to Eq. 11
 - 19: **end if**
 - 20: **end for**
 - 21: **end for**
-

Table 1. Experimental parameters and network architecture for the DDPG agent.

Parameter	Value
Discount factor	0.99
Buffer size	1,000,000
Batch size	64
Actor learning rate	1×10^{-4}
Critic's learning rate	1×10^{-4}
τ (to update target networks)	0.001
O.U. Noise for Δv (mu, theta, sigma)	(0.0, 0.0, 0.2)
O.U. Noise for Δw (mu, theta, sigma)	(0.0, 0.2, 0.3)
Linear speed range	[0, 1] [m/s]
Angular speed range	[-0.5, 0.5] [rad/s]
Actor network (MLP)	6–30–30–2
Critic network (MLP)	(6+2)–30–30–1

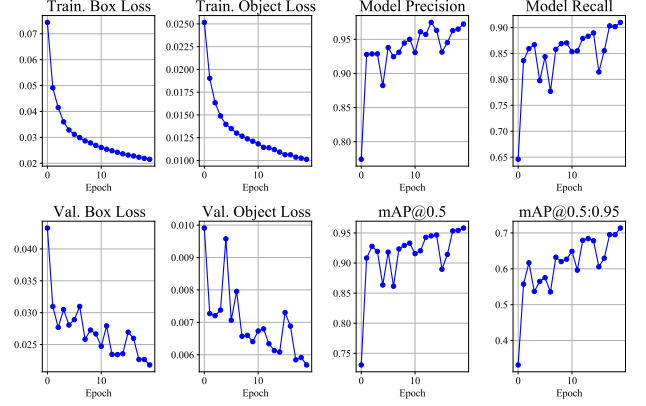
5. Results

This section presents the results achieved after 1) training an event-based pedestrian detector with the PEDRo database, 2) and training an RL-based robotic platform controller using Behavioral Cloning to reduce the agent's initial policy

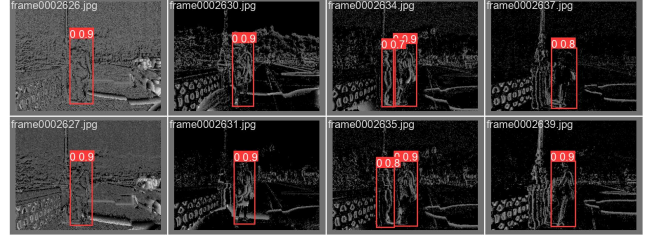
learning time.

5.1. Pedestrian detection based on event cameras

Figure 8 reports the results obtained after training the YOLO network on the PEDRo event-based database for high-speed pedestrian detection.



(a) Learning curves of the YOLO-based pedestrian detector.



(b) Visual samples of the YOLO-based pedestrian detector.

Figure 8. Results after training a YOLOv5s detector on the PEDRo database [4] using the SAE event representation with 10[ms] time window.

Figure 8(a) shows that the loss values for training and validation decrease steadily over epochs, implying that the model is learning to better adjust its predictions for the bounding box and the classification of detected pedestrians. Accuracy and recall metrics show consistent increases, reaching values close to 0.90, offering good performance in detecting and localizing pedestrians on the scene. In addition, the values of $mAP_{0.5}$ and $mAP_{0.5:0.95}$ also increase throughout the training, improving average accuracy for different Intersection over Union thresholds, reaching values above 0.7 in the most demanding mAP (0.5:0.95). On the other hand, the results prove that the use of the SAE event data representation is adequate to detect people with a high level of confidence (0.7-0.9) in pedestrian following, using a 10[ms] time window to generate the representation.

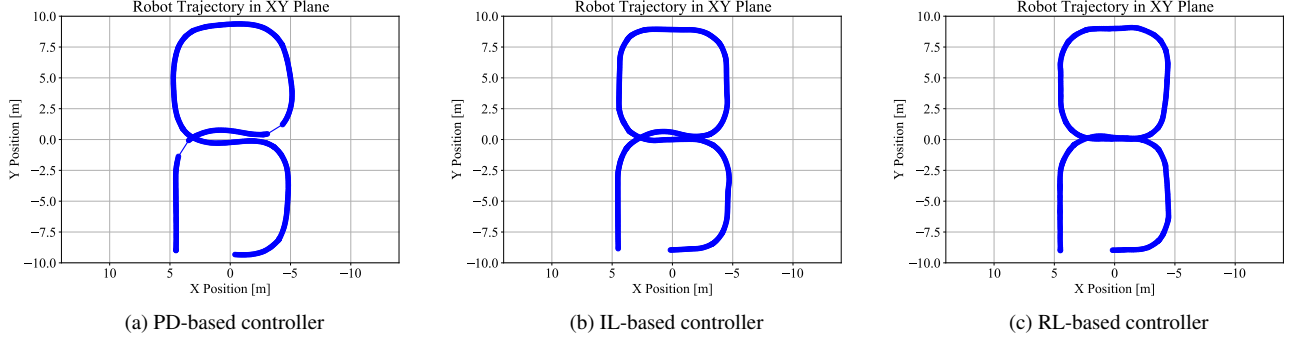


Figure 9. Trajectories described after applying different navigation and human-following controllers using event cameras and other relevant sensors: (a) PD-based controller; (b) Imitation Learning-based controller; (c) Reinforcement Learning-based controller.

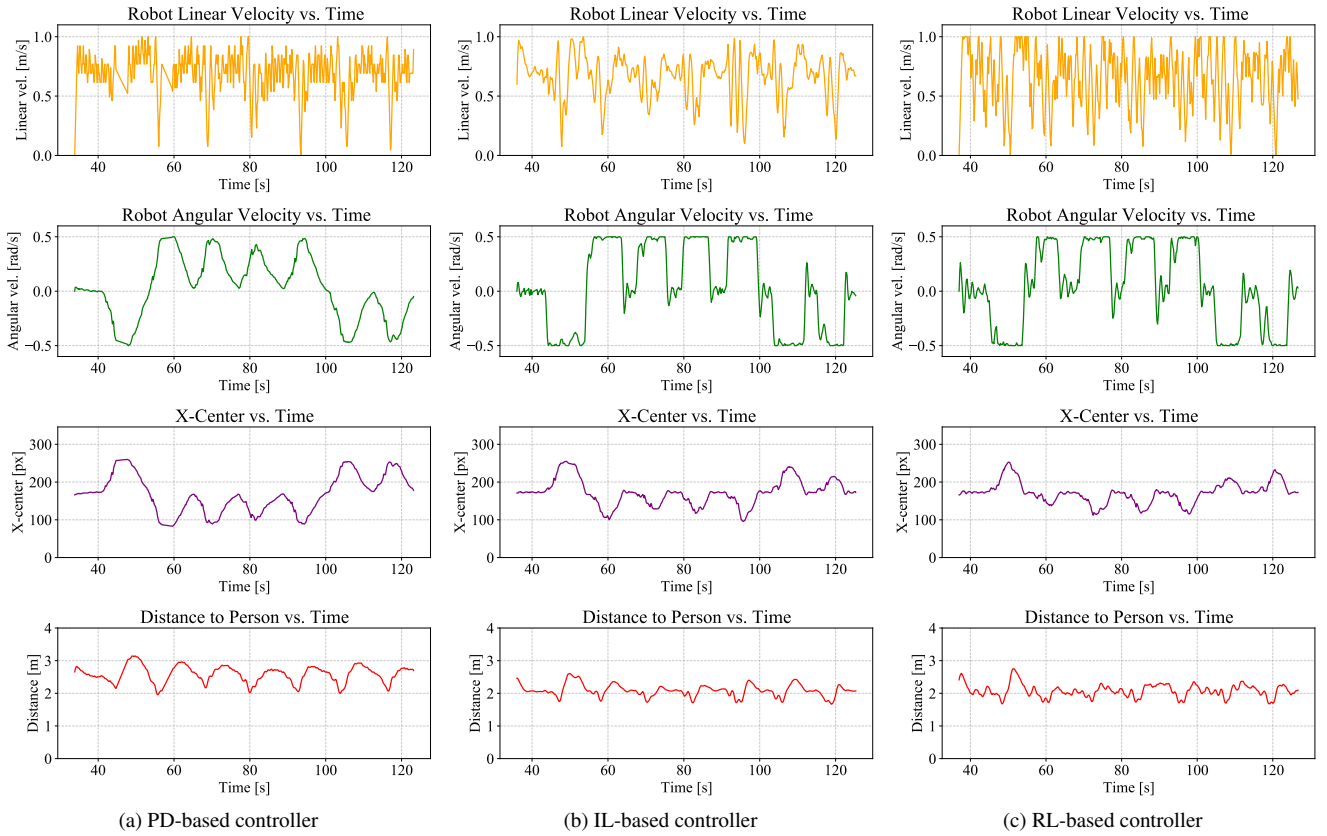


Figure 10. Relevant metrics (robot linear/angular velocity, x-y bounding box estimation, distance-to-person) on navigation and human-following controllers using event cameras and other relevant sensors: (a) PD-based controller; (b) Imitation Learning-based controller; (c) Reinforcement Learning-based controller.

5.2. Evaluation of the navigation algorithms

5.2.1. About the described trajectories

Figure 9 compares the simulated XY trajectories of the Pioneer 3-AT using three control strategies for human-following navigation. The PD-based controller (Fig. 9 (a)) displays considerable deviations, especially in curves, indicating its

limited ability to adapt to rapid changes in direction. The IL controller (Fig. 9 (b)) demonstrates improved stability and follows the target path more closely, though it still shows minor deviations in complex areas, particularly tight curves. This improvement highlights IL's advantage in achieving greater path adherence compared to the PD-based approach, though it has some limitations. The RL controller (Fig. 9 (c))

Table 2. Performance statistics for human-robot navigation controllers: v_r linear velocity, ω_r angular velocity, x_{box} bounding box x-center value, d_{ped} distance to pedestrian.

(a) PD-based Controller				
	v_r [m/s]	ω_r [m/s]	x_{box} [px]	d_{ped} [m]
Mean	0.6923	0.0328	167.0698	2.5889
Median	0.6923	0.0318	167.0000	2.6414
Std. Dev.	0.1782	0.2711	46.9139	0.2587
Min.	0.0000	-0.5000	83.0000	1.9580
Max.	1.0000	0.5000	260.0000	3.1453

(b) IL-based Controller				
	v_r [m/s]	ω_r [m/s]	x_{box} [px]	d_{ped} [m]
Mean	0.6704	0.0349	172.2215	2.0846
Median	0.6977	0.0093	172.0000	2.0737
Std. Dev.	0.1778	0.3795	34.3104	0.1853
Min.	0.0740	-0.5000	96.0000	1.6653
Max.	1.0000	0.5000	255.0000	2.6043

(c) RL-based Controller				
	v_r [m/s]	ω_r [m/s]	x_{box} [px]	d_{ped} [m]
Mean	0.6568	0.0376	171.2376	2.0756
Median	0.6692	0.0279	172.0000	2.0696
Std. Dev.	0.2407	0.3603	27.4392	0.1982
Min.	0.0000	-0.5000	112.0000	1.6754
Max.	1.0000	0.5000	253.0000	2.7543

produces the most accurate trajectory, showing smooth adaptations and effectively managing changes in orientation. This approach achieves precise path-following and a high-speed response to scene conditions.

5.2.2. About the complementary metrics

Table 2 and Figure 10 present the performance metrics for the three control strategies. The analysis considers robot velocity profiles, target centering (x_{box}), and distance to the pedestrian (d_{ped}).

For the PD-based controller (Table 2a, Figure 10a), both linear and angular velocities exhibit high variability, with frequent and abrupt changes. This indicates a reactive behavior, constantly correcting to maintain distance and centering. The X-center fluctuates around a mean of 167 [px], deviating from the true target of 173 [px], while the distance to the person varies between 2 and 3 meters, indicating limited control accuracy.

The Imitation Learning-based controller (Table 2b, Figure 10b) reduces these oscillations moderately. Although still reactive, it shows improved stability in linear motion and smoother angular corrections. The X-center aligns more closely to the 173 [px] target (mean of 172 [px]), and the distance remains consistently closer to 2 [m] than the PD baseline, improving both lateral and longitudinal tracking.

Finally, the Reinforcement Learning-based controller (Table 2c, Figure 10c) achieves the best overall performance, but not without some trade-offs. While its linear velocity presents a higher standard deviation (SD = 0.24) compared to

the PD and IL controllers, the temporal evolution is smoother and more context-driven. Angular velocity shows consistent and controlled adaptation. The X-center stabilizes near 171 [px], closest to the true target of 173 [px], with reduced variance. Similarly, the distance to the pedestrian is well maintained near the 2 [m] goal. These results highlight the RL controller’s ability to adaptively balance precision and stability across different navigation scenarios.

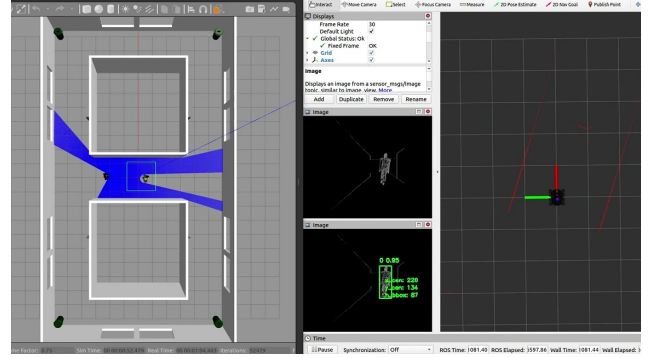


Figure 11. Visual example of the RL-based controller simulated performance for human following. On the right, the figure shows the map rendered in Gazebo. On the left, the RViz software shows the event-based pedestrian detection using SAE and a YOLOv5s detector, the obstacles using a Hokuyo2D, and the Pioneer3AT.

6. Conclusions and Future Work

This work presents the design and implementation of a reinforcement learning-based controller for human-robot navigation using event cameras, depth, and LIDAR data. The proposed system outperforms traditional PD and IL-based approaches in simulation, offering better centering, distance regulation, and adaptation to trajectory changes. These results highlight the potential of event-based sensing for human-centered robotic navigation.

However, the results are not yet definitive. As future work, we aim to develop a complete end-to-end system fully based on event-based perception, capable of operating in real-world conditions. This includes testing in diverse pedestrian motion patterns, extending the evaluation to more complex environments, exploring alternative RL algorithms (e.g., TD3), and studying different rewards. Additional efforts should focus on exploring alternative event-based representations and developing monocular event-based methods for depth and pose estimation to reduce the reliance on multiple sensors.

Acknowledgment

This work was partially supported by the FONDEQUIP project EQM17004 and the Basal project AFB230001. A special mention to Ariel Zuniga (Universidad de O’Higgins) for his support with ROS.

References

- [1] Mohammed Albekairi, Hassen Mekki, Khaled Kaaniche, and Amr Youssef. An innovative collision-free image-based visual servoing method for mobile robot navigation based on the path planning in the image plan. *Sensors*, 23(24), 2023. [1](#)
- [2] Riku Arakawa and Shintaro Shiba. Exploration of reinforcement learning for event camera using car-like robots. *CoRR*, abs/2004.00801, 2020. [2](#)
- [3] Ryad Benosman, Charles Clercq, Xavier Lagorce, Sio-Hoi Ieng, and Chiara Bartolozzi. Event-based visual flow. *IEEE Transactions on Neural Networks and Learning Systems*, 25(2):407–417, 2014. [2, 4](#)
- [4] Chiara Boretti, Philippe Bich, Fabio Pareschi, Luciano Prono, Riccardo Rovatti, and Gianluca Setti. Pedro: an event-based dataset for person detection in robotics. In *IEEE/CVF Conference on Computer Vision and Pattern Recognition Workshops (CVPRW)*, 2023. [4, 6](#)
- [5] Gui Fu, Hongyu Chu, Liwen Liu, Linyi Fang, and Xinyu Zhu. Deep reinforcement learning for the visual servoing control of uavs with fov constraint. *Drones*, 7(6), 2023. [1](#)
- [6] Guillermo Gallego, Tobi Delbrück, Garrick Orchard, Chiara Bartolozzi, Brian Taba, Andrea Censi, Stefan Leutenegger, Andrew J. Davison, Jörg Conradt, Kostas Daniilidis, and Davide Scaramuzza. Event-based vision: A survey. *IEEE Transactions on Pattern Analysis and Machine Intelligence*, 44(1):154–180, 2022. [1, 2](#)
- [7] Xile Gao, Haiyong Luo, Bokun Ning, Fang Zhao, Linfeng Bao, Yilin Gong, Yimin Xiao, and Jinguang Jiang. RI-akf: An adaptive kalman filter navigation algorithm based on reinforcement learning for ground vehicles. *Remote Sensing*, 12(11):1704, 2020. [5](#)
- [8] Lúiza Caetano Garaffa, Maik Basso, Andréa Aparecida Konzen, and Edison Pignaton de Freitas. Reinforcement learning for mobile robotics exploration: A survey. *IEEE Transactions on Neural Networks and Learning Systems*, 34(8):3796–3810, 2023. [1](#)
- [9] Xinyu Hu, Zhihong Liu, Xiangke Wang, Lingjie Yang, and Guanzheng Wang. Event-based obstacle sensing and avoidance for an uav through deep reinforcement learning. In *Artificial Intelligence*, pages 402–413, Cham, 2022. Springer Nature Switzerland. [2](#)
- [10] Yuhuang Hu, Shih-Chii Liu, and Tobi Delbruck. v2e: From video frames to realistic dvs events. In *2021 IEEE/CVF Conference on Computer Vision and Pattern Recognition Workshops (CVPRW)*, pages 1312–1321, 2021. [4](#)
- [11] Zhiyu Huang, Jingda Wu, and Chen Lv. Efficient deep reinforcement learning with imitative expert priors for autonomous driving. *IEEE Transactions on Neural Networks and Learning Systems*, 34(10):7391–7403, 2023. [1](#)
- [12] Zhehao Jin, Jinhui Wu, Andong Liu, Wen-An Zhang, and Li Yu. Policy-based deep reinforcement learning for visual servoing control of mobile robots with visibility constraints. *IEEE Transactions on Industrial Electronics*, 69(2):1898–1908, 2022. [1](#)
- [13] Rahima Khanam, Tahreem Asghar, and Muhammad Hussain. Comparative performance evaluation of yolov5, yolov8, and yolov11 for solar panel defect detection. *Solar*, 5(1), 2025. [4](#)
- [14] Xavier Lagorce, Garrick Orchard, Francesco Galluppi, Bertram E. Shi, and Ryad B. Benosman. Hots: A hierarchy of event-based time-surfaces for pattern recognition. *IEEE Transactions on Pattern Analysis and Machine Intelligence*, 39(7):1346–1359, 2017. [2, 4](#)
- [15] ActivMedia Robotics. Pioneer 3at operations manual. *MobileRobots Inc, Amherst, NH, USA, Tech. Rep*, 3, 2006. [2](#)
- [16] Javier Ruiz-del Solar, Mauricio Correa, Rodrigo Verschae, Fernando Bernuy, Patricio Loncomilla, Mauricio Mascaró, Romina Riquelme, and Felipe Smith. Bender: a general-purpose social robot with human-robot interaction capabilities. *J. Hum.-Robot Interact.*, 1(2):54–75, 2013. [2](#)
- [17] Carlos Sampedro, Alejandro Rodríguez-Ramos, Ignacio Gil, Luis Mejias, and Pascual Campoy. Image-based visual servoing controller for multirotor aerial robots using deep reinforcement learning. In *2018 IEEE/RSJ International Conference on Intelligent Robots and Systems (IROS)*, pages 979–986, 2018. [1](#)
- [18] Chinmay Shinde, Rolif Lima, and Kaushik Das. Deep reinforcement learning based dynamic object detection and tracking from a moving platform. In *2019 Sixth Indian Control Conference (ICC)*, pages 244–249, 2019. [1](#)
- [19] Bharat Singh, Rajesh Kumar, and Vinay Pratap Singh. Reinforcement learning in robotic applications: a comprehensive survey. *Artificial Intelligence Review*, 55(2):945–990, 2022. [1](#)
- [20] Ala Souissi, Hajer Fradi, and Panagiotis Papadakis. Leveraging event streams with deep reinforcement learning for end-to-end uav tracking, 2024. [2](#)
- [21] Rodrigo Verschae and Ignacio Bugueno-Cordova. Event-based gesture and facial expression recognition: A comparative analysis. *IEEE Access*, 11:121269–121283, 2023. [3](#)